Modeling Fabrication Non-Uniformity in Chip-Scale Silicon Photonic Interconnects

Mahdi Nikdast[1,3], Gabriela Nicolescu[1], Jelena Trajkovic[2], and Odile Liboiron-Ladouceur[3]
[1]Polytechnique Montréal, Montréal, Canada [2]Concordia University, Montréal, Canada [3]McGill University, Montréal, Canada
E-mail: mnikdast@ieee.org

***Abstract*—Silicon photonic interconnect (SPI) is a promising candidate for the communication infrastructure in multiprocessor systems-on-chip (MPSoCs). When employing SPIs with wavelength-division multiplexing (WDM), it is required to precisely match different devices, such as photonic switches, filters, etc, in terms of their central wavelengths. Nevertheless, SPIs are vulnerable to fabrication non-uniformity (a.k.a. process variations), which influences the reliability and performance of such systems. Understanding process variations helps develop system design strategies to compensate for the variations, as well as estimate the implementation cost for such compensations. For the first time, this paper presents a computationally efficient and accurate bottom-up method to systematically study different process variations in passive SPIs. Analytical models to study the impact of silicon thickness and waveguide width variations on strip waveguides and microresonator (MR)-based add-drop filters are developed. Numerical simulations are used to evaluate our proposed method. Furthermore, we designed, fabricated, and tested several identical MRs to demonstrate process variations. The proposed method is applied to a case study of a passive WDM-based photonic switch, which is the building block in passive SPIs, to evaluate its optical signal-to-noise ratio (OSNR) under different variations. The efficiency of our proposed method enables its application to large-scale SPIs in MPSoCs, where employing numerical simulations is not feasible.**

I. Introduction

The inter- and intra-chip communication in multiprocessor systems-on-chip (MPSoCs) is progressively growing as a result of integrating an increasingly large number of processing cores on a single die. Silicon photonic interconnect (SPI) is a promising candidate for the communication infrastructure in MPSoCs, introducing high bandwidth, low latency and low power consumption [1]. Moreover, using wavelength-division multiplexing (WDM) technology in SPIs can further boost the bandwidth performance through simultaneous transmission of multiple optical wavelengths on a single waveguide. Several SPIs employing the WDM were proposed, in which microresonators (MRs) and waveguides are the primary building components [2], [3]. Realizing a reliable communication in such interconnects, it is essential to precisely match the central wavelengths among different components. Nevertheless, SPIs are vulnerable to fabrication non-uniformity (a.k.a. process variations), resulting in wavelength mismatches among different components, and hence performance degradation, or in the worst-case, system failure. Process variations stem from the optical lithography process imperfection, in which variations depend on the resist sensitivity, resist age or thickness, exposure change, and etching [4].

Previous work on process variations, including within-die [5], within-wafer [6], [7], and wafer-to-wafer [8] variations demonstrated process variations in silicon photonics fabrication. Particularly, they indicated several nanometers shift in the resonance wavelength of fabricated MRs, and identified silicon thickness variations as the primary driver of the MRs non-uniformity. For instance, [7] demonstrated silicon-on-insulator (SOI) thickness variations of greater than 10 nm across a wafer, which resulted in a $\pm$9 nm shift in the central resonance wavelength of MRs at 1550 nm. Some efforts have been also made to explore process variations at the architecture level. Y. Xu, *et al.* evaluated the bandwidth loss, which was shown to be greater than 40%, in MR-based nanophotonic on-chip networks under process variations [9]. In [10], M. Mohamed, *et al.* proposed a design flow to improve the reliability of the same networks under thermal and process variations. These works, however, failed to comprehensively study process variations in the considered on-chip nanophotonic networks. Also, it is worth mentioning that thermal and process variations are fundamentally different: the thermal variation is a result of thermo-optic effects on silicon photonic devices, while the process variation is caused by the lithography imperfection and etch non-uniformity of photonic devices.

When designing a single photonic device, it is necessary to consider different parameters sweeps, a.k.a. corner analysis, while performing numerical simulations (e.g., the finite-difference time-domain (FDTD) simulations) to predict the behavior of the device after its fabrication. When it comes to large-scale SPIs, however, performing such simulations is not feasible since they impose an extremely high computation cost. This paper, for the first time, presents a computationally efficient and accurate bottom-up method to systematically study the impact of process variations in large-scale passive SPIs. In particular, the novel contributions of this paper are 1) developing comprehensive analytical models to study process variations in strip waveguides; 2) studying the performance of MR-based add-drop filters under process variations; and 3) designing, fabricating, and testing several identical MRs to demonstrate process variations. We consider variations in the silicon thickness and waveguide width. Numerical simulations are considered to evaluate the efficiency and accuracy of our proposed method. As a case study, we apply our method to a passive WDM-based photonic switch, which is the building block in passive SPIs, and evaluate the optical signal-to-noise ratio (OSNR) at its drop port under different process

978-3-9815370-6-2/DATE16/©2016 EDAA

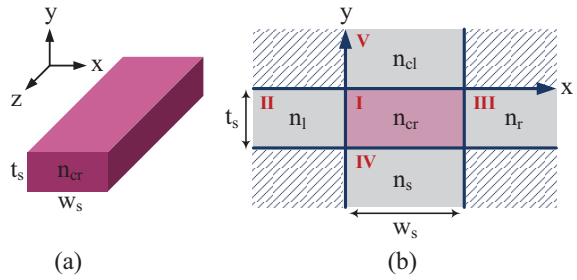

Fig. 1. (a) 3D strip waveguide structure; and, (b) 2D approximation of the strip waveguide.

variations.

The rest of the paper is organized as follows. Section II presents the proposed theory to model process variations in strip waveguides. We study various properties of MR-based add-drop filters under process variations in Section III. Section IV includes quantitative simulation results of our proposed models, as well as evaluations using numerical simulations and our fabrication details. We present a case study of a passive WDM-based photonic switch under various process variations in Section V. Finally, Section VI concludes our work.

II. Process Variations in Basic Components: Strip Waveguides

In this section, we present the primary analyses required to study the propagation constant as well as the effective and group indices of the fundamental transverse electric (TE) mode in strip waveguides under process variations. These parameters determine the propagation of light in photonic components and devices, and hence determine their characteristics. Based on Marcatili's approach, which is an approximate analysis for calculating the propagation modes of waveguides [11], we develop a method to study different process variations in strip waveguides, shown in Fig. 1(a). Our proposed method approximates the 3D strip waveguide structure in Fig. 1(a) with a 2D structure illustrated in Fig. 1(b). The waveguide core, depicted as region I, is from silicon and has a rectangular cross-section with a thickness and width of, respectively, t_s and w_s, while its refractive index is n_{cr}. We consider symmetric strip waveguides in which the homogeneous surrounding regions II, III, IV and V are all from SiO_2, and have equal refractive indices of $n_l = n_r = n_s = n_{cl} = 1.444$.

Considering Fig. 1(b), Maxwell's equations can be applied to fully describe the electromagnetic fields ($E_{x/y}$ and $H_{x/y}$) in terms of the longitudinal field components (E_z and H_z) in each region [12]. As a result, for each region j in this figure we have:

$$E_{x/y} = \frac{-i}{K_j^2}\left(\beta\frac{\partial E_z}{\partial x/y} \text{ +/- } \omega\mu_0\frac{\partial H_z}{\partial y/x}\right), \tag{1a}$$

$$H_{x/y} = \frac{-i}{K_j^2}\left(\beta\frac{\partial H_z}{\partial x/y} \text{ -/+ } \omega\epsilon_0 n_j^2\frac{\partial E_z}{\partial y/x}\right), \tag{1b}$$

where μ_0 and ϵ_0 are the permeability and the permittivity of free-space, respectively. Also, $K_j^2 = n_j^2k_0^2 - \beta^2$, in which k_0 is the free-space wavenumber and is equal to $\frac{2\pi}{\lambda}$, where λ is the optical wavelength. n_j is the refractive index in region j, and β is the propagation constant. ω is the angular frequency and is equal to $\frac{2\pi c}{\lambda}$, in which c is the speed of light in vacuum.

When β is larger than the propagation constant that is allowed in the regions outside region I, then the light is confined in the waveguide core. The longitudinal field components of the modal electromagnetic field in each region are defined in a way that Maxwell's equations are obeyed in all the regions. For region I, these components are in the form of [11]:

$$E_z = a_1 sin\left(k_x(x+\xi)\right) cos\left(k_y(y+\eta)\right), \tag{2a}$$

$$H_z = a_2 cos\left(k_x(x+\xi)\right) sin\left(k_y(y+\eta)\right), \tag{2b}$$

where a_1 and a_2 are the amplitudes, k_x and k_y are the spatial frequencies, and ξ and η are the spatial shifts. Please note that for a symmetric strip waveguide the spatial shifts are small and can be ignored. Applying (2a) and (2b) to (1a) and (1b), the propagation constant in the waveguide core can be calculated as:

$$K_I^2 = n_{cr}^2k_0^2 - \beta^2 = k_x^2 + k_y^2, \tag{3a}$$

$$\beta = \sqrt{n_{cr}^2k_0^2 - k_x^2 - k_y^2}. \tag{3b}$$

Finally, the effective index of the fundamental TE mode in the strip waveguide, n_{eff}, is defined as:

$$n_{eff} = \frac{\beta}{k_0}. \tag{4}$$

Considering the propagation constant and the effective index calculations in (3b) and (4), the spatial frequencies k_x and k_y need to be calculated. Applying the boundary conditions (continuity of the fields) at the I-IV and I-V interfaces, where E_x is parallel to these interfaces, and the boundary conditions at the I-II and I-III interfaces, where E_x is orthogonal to these interfaces, we can find the eigenvalue equations that help calculate the spatial frequencies k_x and k_y. Moreover, the spatial frequencies depend on the width and thickness of the waveguide. In this paper, we define ρ_t and ρ_w to take into account the variations in the silicon thickness and waveguide width, respectively. Employing these parameters and respecting the boundary conditions, k_x and k_y can be calculated using the following eigenvalue equations:

$$e_{v1}(\lambda, W_s) = tan\left(k_xW_s\right) - \frac{n_{cr}^2k_x\left(n_r^2\gamma_l + n_l^2\gamma_r\right)}{n_l^2n_r^2k_x^2 - n_{cr}^4\gamma_l\gamma_r}, \tag{5a}$$

$$e_{v2}(\lambda, T_s) = tan\left(k_yT_s\right) - \frac{k_y\left(\gamma_s + \gamma_{cl}\right)}{k_y^2 - \gamma_s\gamma_{cl}}, \tag{5b}$$

where,

$$T_s = t_s \pm \rho_t, \tag{5c}$$

$$W_s = w_s \pm \rho_w, \tag{5d}$$

$$\gamma_{l/r}^2 = \left(n_{cr}^2 - n_{l/r}^2\right)k_0^2 - k_x^2, \tag{5e}$$

$$\gamma_{s/cl}^2 = \left(n_{cr}^2 - n_{s/cl}^2\right)k_0^2 - k_y^2. \tag{5f}$$

k_x and k_y can be calculated by solving (5a) and (5b), i.e. $e_{v1} = 0$ and $e_{v2} = 0$.

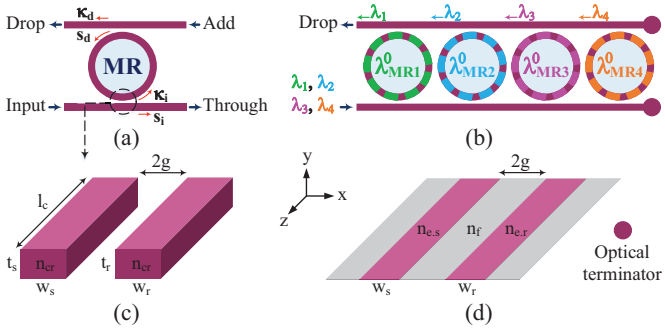

Fig. 2. (a) MR-based add-drop filter structure; (b) Passive WDM-based photonic switch; (c) 3D directional coupler model for the coupling region in MR-based add-drop filters; and, (d) 2D approximation of the coupler.

In order to accurately calculate the effective and group indices of a strip waveguide, we need to take into account the impact of material and waveguide dispersion (chromatic dispersion). Material dispersion occurs since the material refractive index, silicon in this case, depends on the wavelength. Also, the wavelength-dependency of the propagation constant in a waveguide results in the waveguide dispersion. In this paper, we model the chromatic dispersion using the Sellmeier equation, which provides an empirical relationship between the refractive index of a medium and the light's wavelength [13]. As the light is mostly confined in the waveguide core, we can ignore the dispersion in the substrate and cladding (regions IV and V). The Sellmeier equation for silicon can be written as:

$$n_{cr}^2(\lambda) = 1 + \frac{10.67\lambda^2}{\lambda^2 - 0.31} + \frac{0.003\lambda^2}{\lambda^2 - 1.13} + \frac{1.54\lambda^2}{\lambda^2 - 1104^2}. \quad (6)$$

Considering the propagation constant calculation in (3b), the effective index of a strip waveguide under silicon thickness and waveguide width variations, and when the optical wavelength is λ is calculated in:

$$n_{eff}(T_s, W_s, \lambda) = \frac{\lambda}{2\pi}\sqrt{n_{cr}^2(\lambda)k_0^2 - k_x^2(T_s, W_s, \lambda) - k_y^2(T_s, W_s, \lambda)}. \quad (7)$$

Please note that based on (5a) and (5b), k_x and k_y depend on the waveguide thickness, width, and optical wavelength in (7). Considering both the material and waveguide dispersion and the effective index definition in (7), the group index, n_g, of a strip waveguide can be defined as:

$$n_g(T_s, W_s, \lambda) = n_{eff}(T_s, W_s, \lambda) - \lambda\frac{dn_{eff}(T_s, W_s, \lambda)}{d\lambda}. \quad (8)$$

III. Process Variations in Photonic Devices: MR-based Add-Drop Filters

Leveraging the proposed analytical models in the previous section, we study the impact of process variations on MR-based add-drop filters in this section. In this paper, we consider racetrack microresonators and for simplicity we refer to them as MRs. MR-based add-drop filters are the basic building blocks in passive SPIs which can, when on resonance, switch/drop an optical signal (from the input to the drop port in Fig. 2(a)) or let it pass (from the input to the through port).

A. Resonance Wavelength Shift

Fig. 2(a) depicts the structure of an MR-based add-drop filter. As the figure indicates, a portion of the input optical signal couples to the MR with a cross-over coupling coefficient of κ_i, and then it couples to the drop waveguide with a coupling coefficient of κ_d. Similarly, the uncoupled light continues propagating towards the through port and inside the MR with straight-through coefficients of s_i and s_d, respectively [14]. In this paper, we assume that the input and drop waveguides are symmetrically coupled to the MR, i.e. $\kappa_i = \kappa_d$ and $s_i = s_d$.

When the round-trip optical phase, ϕ_{rt}, is an integer multiple of 2π, the MR is on resonance (it drops the input signal):

$$\phi_{rt}(T_r, W_r, \lambda_{MR}) = \frac{2\pi n_{eff}(T_r, W_r, \lambda_{MR})L_{rt}(T_r, W_r)}{\lambda_{MR}} = m2\pi, \quad (9)$$

in which T_r and W_r, respectively, indicate the thickness and width of the MR's waveguide under variations, which can be defined similar to (5c) and (5d). We can safely assume that $T_r = T_s$ and $W_r = W_s$, i.e. while $t_r = t_s$ and $w_r = w_s$, the variations in the input waveguide and the MR are also the same. λ_{MR} is the resonance wavelength. Also, L_{rt} is the round-trip length of the MR that equals $2\pi r + 2l_c$, where r is the MR's radius and l_c is the coupler length (see Fig. 2(c)). It is worth mentioning that the effective and group indices of the MR can be calculated using the input waveguide. Fig. 2(b) indicates a passive WDM-based photonic switch in which the MRs are on resonance, i.e. optical signals on different wavelengths, which are matched with the resonance wavelengths of the MRs, are dropped.

Process variations can change the resonance wavelength of MRs. Considering the first order approximation of the waveguide dispersion and the relations in (8) and (9), the resonance wavelength shift, $\Delta\lambda_{MR}$, is calculated as:

$$\Delta\lambda_{MR}(T_r, W_r, \lambda_{MR}^0) = \frac{\Delta_{\rho_{t/w}} n_{eff}\lambda_{MR}^0}{n_g(t_r, w_r, \lambda_{MR}^0)}, \quad (10)$$

where $\Delta_{\rho_{t/w}} n_{eff}$ includes the changes in the effective index due to the thickness or waveguide width variations. Also, λ_{MR}^0 is the initial resonance wavelength with no variations.

B. Optical Spectrum of MR-based Add-Drop Filters

Studying the cross-over and straight-through coefficients, $\kappa_{i/d}$ and $s_{i/d}$, we model the coupling region in Fig. 2(a), the region specified by a dashed circle, in Fig. 2(c). As the figure indicates, the coupling region can be studied by considering a directional coupler (DC), in which two identical strip waveguides are in close proximity. The gap between the two waveguides is $2g$, which decreases (increases) as the waveguides get wider (narrower). We analytically calculate the cross-over length, L_c, and the coefficients using the supermode theory [4], [15]. The cross-over length is a length over which the optical power completely couples from one waveguide to the other one after a π phase shift difference. As a result, for any length l_c shorter than L_c, a fraction of the optical power,

i.e. $\kappa^2_{i/d}$, couples from one waveguide to the other one, while the rest of the power, i.e. $s^2_{i/d}$, remains in the first waveguide.

According to the supermode analysis, the effective indices of the first two eigenmodes of the coupled waveguides, which are known as symmetric (even) and antisymmetric (odd) modes, determine the cross-over length and coupling coefficients in a DC. Given that the effective indices of the symmetric and antisymmetric modes are, respectively, n_{sm} and n_{asm}, the cross-over length can be calculated as:

$$L_c(T_r, W_r, \lambda) = \frac{\lambda}{2\left(n_{sm}(T_r, W_r, \lambda) - n_{asm}(T_r, W_r, \lambda)\right)}, \tag{11}$$

in which $n_{sm} > n_{asm}$. Accordingly, the coupling coefficients can be analyzed as:

$$\kappa_{i/d}(T_r, W_r, \lambda) = \left| sin\left(\frac{\pi}{2L_c(T_r, W_r, \lambda)} l_c\right)\right|, \tag{12}$$

where l_c is the length of the coupler. We assume a lossless coupler in which $|\kappa_{i/d}|^2 + |s_{i/d}|^2 = 1$, but the optical losses of the coupler are included in the round-trip loss of the entire optical cavity. Calculating n_{sm} and n_{asm}, we approximate the 3D DC in Fig. 2(c) with the 2D structure shown in Fig. 2(d). In this figure, $n_{e.s} = n_{e.r}$ is the effective index of the slab waveguide of a thickness T_r in the y direction in Fig. 2(c), which can be calculated using the proposed method in the previous section. Furthermore, we consider $n_f = 1.444$. Finally, the effective index of the symmetric supermode can be calculated using the following eigenvalue equation:

$$e_{v3}(\lambda, W_r, g) =$$

$$tan(2N_1) - \frac{N_1 N_2\left(1 + tanh(2N_2 g W_r^{-1})\right)}{N_1^2 - N_2^2 tanh\left(2N_2 g W_r^{-1}\right)}, \tag{13a}$$

$$2N_1 = k_0 W_r \sqrt{n_{e.r}^2 - (\beta/k_0)^2}, \tag{13b}$$

$$2N_2 = k_0 W_r \sqrt{(\beta/k_0)^2 - n_f^2}, \tag{13c}$$

in which for the antisymmetric mode $tanh$ should be replaced by $coth$ [16].

Employing the coupling coefficients, we can analyze the through and drop ports' responses in MR-based add-drop filters. The through port response is given by:

$$T(T_r, W_r, \lambda) = \frac{s_{i/d}(T_r, W_r, \lambda)\left(1 - \sqrt{A}e^{i\phi_{rt}}\right)}{1 - \sqrt{A}s^2_{i/d}(T_r, W_r, \lambda)e^{i\phi_{rt}}}, \tag{14a}$$

while the response of the drop port can be defined as:

$$D(T_r, W_r, \lambda) = \frac{-\kappa^2_{i/d}(T_r, W_r, \lambda)A^{1/4}e^{i\phi_{rt}/2}}{1 - \sqrt{A}s^2_{i/d}(T_r, W_r, \lambda)e^{i\phi_{rt}}}. \tag{14b}$$

In these equations, A is the power attenuation that can be calculated as $A(T_r, W_r) = e^{-\alpha L_{rt}(T_r, W_r)}$, in which α is the propagation loss of the waveguide in dB/cm. Please note that the total round-trip phase, ϕ_{rt}, includes the phase accumulated in the light propagating in the coupler. Moreover, as can be seen from (14a) and (14b), all the parameters that determine the optical spectrum of an MR-based add-drop filter are affected by process variations (see also (9) and (12)).

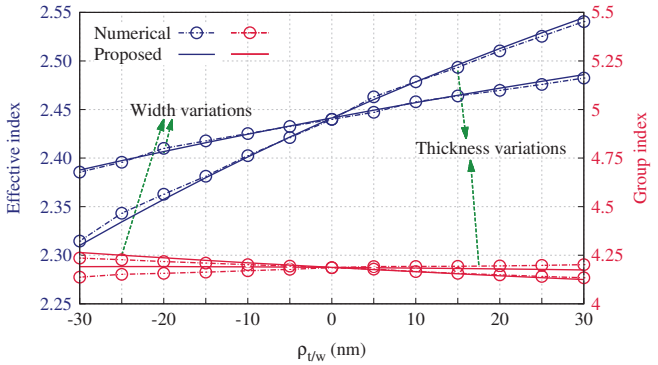

Fig. 3. Effective and group indices of a strip waveguide calculated using the proposed method (solid line), and MODE (dashed lines with circles) under different variations.

IV. Results, Evaluations, and Fabrication

In this section, we quantitatively simulate our proposed models in MATLAB. Evaluating the proposed method, we perform numerical simulations in MODE, which is a commercial-grade simulator eigenmode solver and propagator [17]. Moreover, our fabrication and its results are detailed in this section. We consider $w_s = w_r = 500$ nm and $t_s = t_r = 220$ nm, which are currently a standard in silicon photonics fabrication. Also, a variation range of ± 30 nm is considered in our simulations, i.e. $\rho_{t/w} \in$[-30, 30] nm. Furthermore, similar to our fabrication, we consider the central laser wavelength, λ, and the gap, $2g$, to be 1550 nm and 200 nm, respectively. In this paper, we assume that $\alpha = 1$ dB/cm.

A. Quantitative Simulation Results

Employing (7) and (8), Fig. 3 indicates the impact of silicon thickness and waveguide width variations on the effective and group indices of a strip waveguide. As the figure shows, when $\rho_{t/w}$ increases, the effective index (group index) increases (slightly decreases). Considering the analytical models developed to study the resonance wavelength shift in (9) and (10), Fig. 4(a) indicates the resonance wavelength shift in MR-based add-drop filters under different variations. Please note that the resonance wavelength shift indicated in Fig. 4(a) does not depend on the MR's radius. Both Figs. 3 and 4(a) include the numerical simulation results from MODE, compared to which our method indicates a very high accuracy (error rate <1%). Also, within the considered variation range, thickness variations impose larger deviations: thickness variations result in a total resonance wavelength shift of ≈90 nm in Fig. 4(a).

Considering (12), (14a), and (14b), Figs. 4(b) and 4(c) indicate the through and drop ports responses in an MR-based add-drop filter for $\rho_{t/w} = \pm 10$ nm, in which $r \approx 9$ μm and $l_c = 4$ μm considered to better indicate the shifts. Also, for better illustration, we excluded the numerical simulation results in the figure, but the error rate is still <1% (compare the simulation results in Fig. 5(b)). The initial resonance wavelength, λ^0_{MR}, is at 1550 nm, and the free-spectral range (FSR) is ≈9 nm. As can be seen, when $\rho_{t/w} > 0$, there is a red-shift in the resonance wavelength, while $\rho_{t/w} < 0$ results

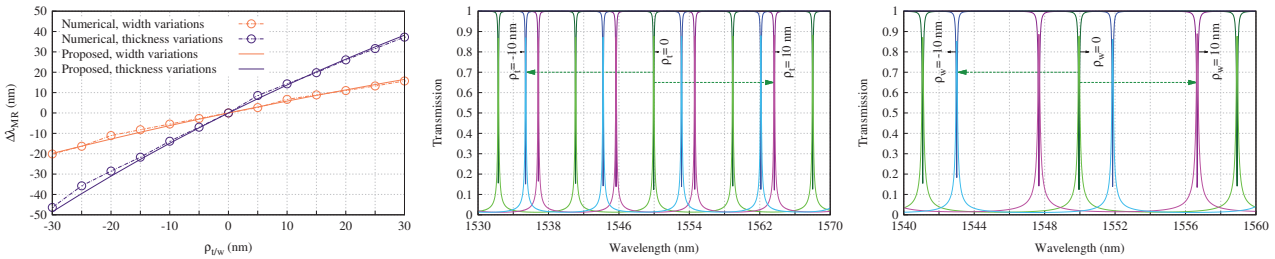

(a) Resonance wavelength shift (b) $\rho_t = \pm 10$ nm ($\rho_w = 0$) (c) $\rho_w = \pm 10$ nm ($\rho_t = 0$)

Fig. 4. (a) Resonance wavelength shift in MR-based add-drop filters under different variations; and, (b) and (c): Optical spectrum of an MR-based add-drop filter when $\rho_{t/w} = \pm 10$ nm calculated using the proposed method.

in a blue-shift in the resonance wavelength. Furthermore, in Fig. 4(b), the resonance wavelength shift is larger than the FSR, i.e. $\Delta\lambda_{MR}$ >FSR. Another important observation is that there is a good agreement between the results in Fig. 4(a), which is based on (10), and those indicated in Figs. 4(b) and 4(c). In both Figs. 3 and 4, and using the same computing platform, the proposed method computed the results in a few seconds, while the numerical simulation took more than an hour to complete (>100× improvement). All the results indicate the severe impact of silicon thickness variations, which is in agreement with the demonstrations in [5]–[7].

B. Fabrication Results

We designed an MR to demonstrate the impact of process variations. Several (30 in total) identical copies of the designed MR were placed on a 2×1 mm^2 chip fabricated by the Electron Beam (EBeam) Lithography System at the University of Washington. The unit cell of the designed MR with a pair of fiber grating couplers, which are designed for 1550 nm quasi-TE operation and located on a 127 μm pitch, is depicted in Fig. 5(a). Our design includes 220 nm thick SOI strip waveguides with a 500 nm width connected to a TE polarization MR with a 10 μm radius, and a coupler length and gap of ≈1 μm and 200 nm, respectively. The MRs were located in the middle of the chip along the 2 mm length and with an equal distance of 60 μm.

Using an automated testing facility, we carefully tested all the MRs and the results are indicated in Fig. 5(b). Furthermore, during the test process, the chip was located on a thermal heater to eliminate the thermal variations. As the figure shows, although all the MRs are identically designed, there is a variation in the resonance wavelengths of the MRs placed in different locations of the chip. The optical spectrum (through port response) of the designed MR is simulated using MODE and our proposed method considering $\rho_{t/w} = 0$. Comparing the fabrication and simulation results, we can see that, in the worst-case, there is a ≈2 nm shift in the resonance wavelength of the MR. This shift can be attributed to the thickness (width) variation of 2 nm (3 nm). Comparing all the MRs within the same distance, we found out that the differences in the resonance wavelengths increase with the distance among MRs. The same conclusion was demonstrated in [5], [8].

It is worth mentioning that the mask-less EBeam lithography has a high resolution, but a low throughput, limiting its

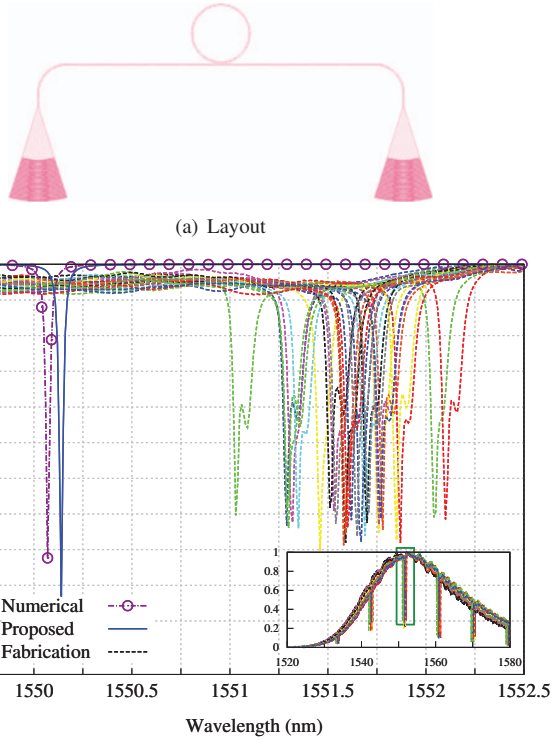

(a) Layout

(b) Measured results

Fig. 5. (a) Layout of the fabricated MR; and, (b) Fabrication results obtained by automatically testing several identically designed MRs, as well as the simulation results from MODE and the proposed method both with $\rho_{t/w} = 0$.

usage to low-volume production of semiconductor devices, and research and development. Other works that considered mask-based optical lithography demonstrated much larger resonance wavelength shifts in MRs due to process variations (see our discussion in the introduction). However, even with a small variation, the performance of the system can be highly affected, as we will indicate in the next section.

V. Case Study

This section presents a case study of a passive WDM-based photonic switch consisting of four MRs, shown in Fig. 2(b). The proposed case study is the building block in passive SPIs. We consider a channel spacing of 4 nm, where $\lambda_1 = \lambda^0_{MR1} =$ 1550 nm and $\lambda_4 = \lambda^0_{MR4} = 1562$ nm. Also, the radius of the MRs is 5 μm, while each MR's radius is slightly different to

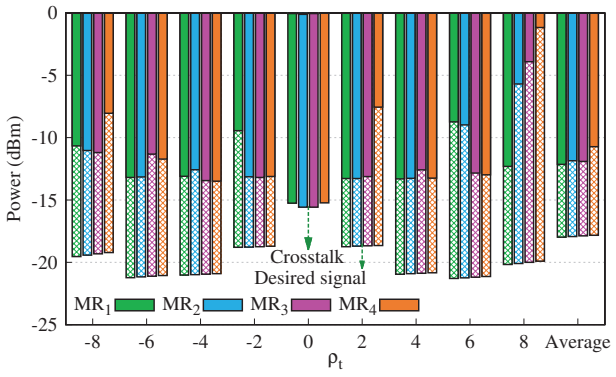

(a) Thickness variations ($\rho_w = 0$)

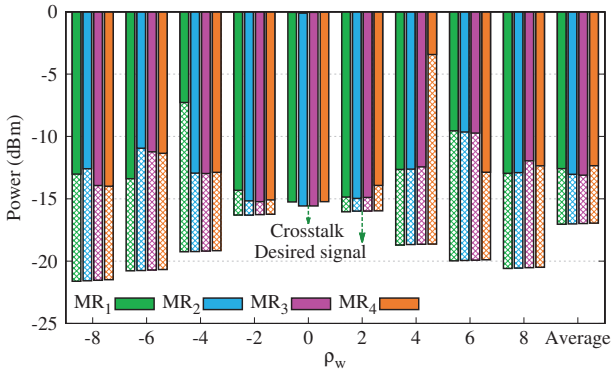

(b) Width variations ($\rho_t = 0$)

Fig. 6. Crosstalk and desired signal power (their difference is the OSNR in dB) for each input optical wavelength in Fig. 2(b) under different variations.

match the considered resonance wavelengths. Moreover, for all the MRs $l_c = 3$ μm and $2g = 200$ nm. Two optical terminators (e.g., waveguide tapers) are located on the add and through ports to avoid any reflections.

When the resonance wavelength shifts, the dropped signal power, which is the desired signal, decreases. Also, crosstalk noise from the neighboring channels interferes with the desired signal [18]. Employing (14a) and (14b), we define the OSNR (in dB) as the difference between the desired signal power and the power of the crosstalk noise corrupting that signal at the drop port. Results are indicated in Figs. 6(a) and 6(b), in which the input optical power is 0 dBm. Our simulations include both the coherent and incoherent crosstalk noise. For simplicity, the variation range, $\rho_{t/w} \in$[-8, 8] nm, is considered in a way to make sure that $\Delta\lambda_{MRi}$<FSR= 15 nm for $i = 1, 2, 3, 4$. As the figures show, when $\rho_{t/w} = 0$, the desired signal power is high and the crosstalk noise power is low, and hence the OSNR is high. When variations are introduced, however, the OSNR drops sharply, which is the result of lower desired signal and higher crosstalk noise power. Considering Fig. 6, on average, the desired signal power decreases by 18 dB (17 dB) under the considered silicon thickness (waveguide width) variations. Similarly, the crosstalk noise power increases by 4 dB (3 dB) under the silicon thickness (waveguide width) variations. Consequently, the OSNR drops by 22 dB and 20 dB under the silicon thickness and waveguide width variations, respectively.

VI. Conclusion

This paper develops a computationally efficient and accurate bottom-up approach to systematically study process variations in passive silicon photonic interconnects. We comprehensively study strip waveguides and MR-based add-drop filters under the silicon thickness and waveguide width variations. The accuracy of our proposed models are evaluated using time-consuming numerical simulations, and we indicate an error rate of <1% with >100× improvement in the computation time. Moreover, our study involves fabrication results to demonstrate process variations. Employing the developed method, we indicate a considerable reduction in the OSNR of a passive WDM-based photonic switch as the result of process variations. The low complexity of our proposed method enables the system designer to evaluate large-scale photonic interconnects in MPSoCs under process variations, for which the employment of numerical simulations is not feasible.

Acknowledgment

We acknowledge SiEPIC, ReSMiQ, and NSERC for funding this project, and UBC for the automated measurements.

References

[1] M. Fiorentino, Z. Peng *et al.*, "Devices and architectures for large scale integrated silicon photonics circuits," in *IEEE WTM*, Jan. 2011.
[2] Y. Pan, J. Kim *et al.*, "FlexiShare: channel sharing for an energy-efficient nanophotonic crossbar," in *HPCA*, Jan. 2010.
[3] S. Le Beux, J. Trajkovic *et al.*, "Optical ring network-on-chip (ORNoC): architecture and design methodology," in *DATE*, March 2011.
[4] L. Chrostowski and M. Hochberg, *Silicon photonics design from devices to systems*. Cambridge University Press, May 2015.
[5] L. Chrostowski, X. Wang *et al.*, "Impact of fabrication non-uniformity on chip-scale silicon photonic integrated circuits," in *OFC*, March 2014.
[6] S. Selvaraja, W. Bogaerts *et al.*, "Subnanometer linewidth uniformity in silicon nanophotonic waveguide devices using CMOS fabrication technology," *IEEE Journal of Selected Topics in Quantum Electronics*, vol. 16, no. 1, pp. 316–324, Jan. 2010.
[7] W. A. Zortman, D. C. Trotter *et al.*, "Silicon photonics manufacturing," *Optical Express*, vol. 18, no. 23, pp. 598–607, Nov. 2010.
[8] X. Chen, M. Mohamed *et al.*, "Process variation in silicon photonic devices," *Applied Optics*, vol. 52, no. 31, pp. 7638–7647, Nov. 2013.
[9] Y. Xu, J. Yang *et al.*, "Tolerating process variations in nanophotonic on-chip networks," in *ISCA*, June 2012.
[10] M. Mohamed, Z. Li *et al.*, "Reliability-aware design flow for silicon photonics on-chip interconnect," *IEEE TVLSI*, vol. 22, no. 8, pp. 1763–1776, Aug. 2014.
[11] W. J. Westerveld, S. M. Leinders *et al.*, "Extension of Marcatili's analytical approach for rectangular silicon optical waveguides," *Journal of Lightwave Technology*, vol. 30, no. 14, pp. 2388–2401, July 2012.
[12] A. Yariv and P. Yeh, *Photonics: optical electronics in modern communications*. Oxford University Press, 2007.
[13] D. F. Edwards and E. Ochoa, "Infrared refractive index of silicon," *Applied Optics*, vol. 19, no. 24, pp. 4130–4131, Dec. 1980.
[14] W. Bogaerts, P. De Heyn *et al.*, "Silicon microring resonators," *Laser and Photonics Reviews*, vol. 6, no. 1, pp. 47–73, 2012.
[15] W. S. C. Chang, *Principles of optics for engineers*. Cambridge University Press, 2015.
[16] K. S. Chiang, "Integrated optic waveguides," *Wiley Encyclopedia of Electrical and Electronics Engineering*, 2001.
[17] Lumerical Solutions, Inc. [Online]. Available: http://www.lumerical.com/tcad-products/mode/
[18] M. Nikdast, J. Xu *et al.*, "Crosstalk noise in WDM-based optical networks-on-chip: a formal study and comparison," *IEEE TVLSI*, vol. 23, no. 11, pp. 2552–2565, Nov. 2015.